Check for updates

RESEARCH ARTICLE

Key Points:
- Observations from five polar-orbiting satellites are used to derive TB temporal variation at 19 GHz
- TB temporal variation at 19 GHz correlates well with the instantaneous precipitation rate
- TB temporal variation at 19 GHz primarily reflects the surface emissivity variation due to the precipitation impact

Correspondence to:
Y. You,
yyou@umd.edu

The Instantaneous Retrieval of Precipitation Over Land by Temporal Variation at 19 GHz

Yalei You[1] [ID], **Christa Peters-Lidard[2]** [ID], **Nai-Yu Wang[1]**, **Joseph Turk[3]** [ID], **Sarah Ringerud[1,2]**, **Song Yang[4]** [ID], and **Ralph Ferraro[5]**

[1]Earth System Science Interdisciplinary Center/Cooperative Institute for Climate and Satellites, University of Maryland, College Park, MD, USA, [2]Hydrological Sciences Laboratory, NASA Goddard Space Flight Center, Greenbelt, MD, USA, [3]Jet Propulsion Laboratory, California Institute of Technology, Pasadena, CA, USA, [4]Naval Research Laboratory, Monterey, CA, USA, [5]NOAA/NESDIS/STAR, College Park, MD, USA

Abstract The primary signal used in all current passive microwave precipitation retrieval algorithms over land is the depression of the instantaneous brightness temperature (TB) caused by ice scattering. This study presents a new methodology to retrieve instantaneous precipitation rate over land by using TB temporal variation (ΔTB) at 19 GHz, which primarily reflects the surface emissivity variation due to the precipitation impact. As a proof-of-concept, we exploit observations from five polar-orbiting satellites over the Southern Great Plains of the United States. Results show that ΔTB at 19 GHz correlate well with the instantaneous precipitation rate. Further analysis shows that ΔTB at 19 GHz is better correlated with the precipitation rate when multiple satellite observations are used due to the much shorter revisit time for a certain location. The retrieved instantaneous precipitation rate over Southern Great Plains from ΔTB at 19 GHz reasonably agrees with the surface radar observations, with the correlation, the root-mean-square error and the bias being 0.49, 2.39 mm/hr, and 6.54%, respectively. Future work seeks to combine the ice scattering signal at high frequencies and this surface emissivity variation signal at low frequencies to achieve an optimal retrieval performance.

Plain Language Summary Current precipitation estimation technique via satellite passive microwave observations links the hydrometers in the air to the surface precipitation intensity. That is, the cold brightness temperature (TB) at high-frequency channels (e.g., 85 GHz) indicates heavy precipitation. The TB observations from low-frequency channels such as 19 GHz are largely discounted. This study presents a new idea to link the surface condition variation to the precipitation intensity, by using TB temporal variation (δTB) at 19 GHz from five polar-orbiting satellites. Results show that δTB at 19 GHz correlate well with the precipitation rate. The estimated instantaneous precipitation rate over the Southern Great Plains of United States from δTB at 19 GHz reasonably agrees with the ground radar observations, with the correlation, the root-mean-square error, and the bias at 0.49, 2.39 mm/hr, and 6.54%, respectively.

1. Introduction

Instantaneous precipitation rate retrieval by passive microwave radiometers over land is very challenging. Over the ocean where the microwave emissivity is low, the brightness temperature (TB) increase due to the radiometrically *warm* raindrops is apparent. However, the high surface emissivity over land largely masks the information from liquid water (e.g., Ferraro et al., 1994; Wang et al., 2009; Wilheit, 1986; You et al., 2014). In addition, the land surface emissivity is highly inhomogeneous, which makes it difficult to physically model the land surface emissivity accurately on the global scale Tian et al. (2015).

Despite these challenges, precipitation retrieval algorithms have been successfully developed and implemented for several decades over land. For example, some algorithms directly establish a relation between satellite observed TB at high-frequency channels (e.g., 85 GHz) and precipitation rate through various statistical techniques, including regression (Ferraro & Marks, 1995; Laviola & Levizzani, 2011; McCollum & Ferraro, 2003; Wang et al., 2009), neural networks (Islam et al., 2014; Staelin & Chen, 2000), and Bayes' theorem (Petty & Li, 2013; You et al., 2015, 2016). The reference precipitation rates are usually from surface radar observations (Ferraro & Marks, 1995; You et al., 2015, 2016), ground gauge observations (Kongoli et al., 2015), or spaceborne

precipitation radar observations (Islam et al., 2014; Petty & Li, 2013; Wang et al., 2009). Precipitation retrieval algorithms have also been developed by including the radiative transfer model (e.g., Aonashi et al., 2009; Kidd et al., 2016; Kummerow et al., 2015; G. Liu & Curry, 1992; Sano et al., 2013; Seo et al., 2016). Often, the radiative transfer model is employed to simulate the observed TBs. To do the simulation, the hydrometeor profiles are either derived from a cloud-resolving model (Kidd et al., 2016; Sano et al., 2013) or satellite-based precipitation radar observations (Kummerow et al., 2015).

These precipitation retrieval algorithms differ greatly in detail. However, they share one common feature: linking the scattering signal from the hydrometeors aloft to the precipitation at the surface (Petty, 1995; You et al., 2011; You, Wang, et al., 2017).

This study demonstrates later that TB temporal variation (ΔTB) at 19 GHz, primarily the surface emissivity variation signal, is well correlated with the precipitation rate. Therefore, it provides a new technique to retrieve precipitation rate over land from satellite microwave observations. Using observations from eight polar-orbiting satellites, You, Peters-Lidard, et al. (2017) recently showed that ΔTB at high-frequency channels (e.g., 89 and 183 ± 7 GHz) can significantly improve the precipitation retrieval performance over snow-covered areas, by minimizing the surface emissivity variation influence. In contrast, this study utilizes the surface emissivity variation signal contained in the TB temporal variation at 19 GHz to retrieve precipitation rate.

Previous works have used the surface emissivity and soil moisture to estimate the precipitation rate. For example, You et al. (2014) estimated the rainfall rate using the emissivity at 10 GHz in a case study over the Southern Great Plains (SGP) of the United States. Brocca et al. (2014) demonstrated that it is possible to estimate the surface rain rate from soil moisture variation. Koster et al. (2016) applied this method (converting soil moisture to rain rate) globally, using soil moisture products from the Soil Moisture Active Passive mission, the Soil Moisture and Ocean Salinity satellite mission, and the Advanced Scatterometer mission. They concluded that the estimated rain rates are, on average, highly correlated with the in situ gauge-observed rain rates with a square of the correlation coefficient of 0.6, at the 100 km and 5-day resolution. Birman et al. (2015) showed that the daily rainfall estimation from surface emissivity at 89 GHz agrees reasonably well with surface gauge observations in France. Incorporating soil moisture information to correct the satellite rainfall accumulation estimates has been documented to reduce errors (Crow et al., 2009; Pellarin et al., 2013).

Key differences between these works and the current study are the following: (1) Previous studies based on the emissivity and soil moisture are retrieving precipitation accumulation (e.g., daily). However, this study is attempting to retrieve the instantaneous precipitation, which is a much more challenging issue. (2) This study exploits TB temporal variation to retrieve the precipitation rate, which significantly alleviates surface contamination (details in following sections). And (3) we use a satellite constellation (five satellites) in this study to obtain a reasonably high temporal resolution from microwave radiometer observations.

It is known that low-frequency channels (e.g., 10, 19, and 37 GHz) have a poorer spatial resolution compared with the high-frequency channels (e.g., 89 GHz). Nevertheless, they are more sensitive to the surface emissivity change due to the precipitation impacts. The purpose of this study is not to show that the low-frequency channels can replace the high-frequency channels. Rather, we show that TB temporal variation at 19 GHz primarily reflects the surface emissivity variation due to the precipitation impacts, which may complement the ice scattering signals from high-frequency channels in future precipitation algorithm development. In addition, we choose 19 GHz because it is the lowest frequency commonly available from the five satellites used in the current study. Therefore, it is most sensitive to the surface characteristics, compared with other commonly available frequencies (e.g., 37 and 89 GHz).

We would like to emphasize that this study does not directly use 19 GHz itself to retrieve the instantaneous rain rate. Instead, we use the temporal variation of 19 GHz from five satellites, which is well correlated with the instantaneous rain rate. Additionally, it is known that the 19-GHz channel does not necessarily perform better than the 89-GHz channel over land, and our later analysis shows this point. However, it does have its merits in providing additional information, for example, when the 89 GHz is not available (e.g., WindSat).

The data used in this study are described in section 2. The methodology, including the definition of the TB temporal variation, is provided in section 3. Section 4 begins with a case study to show the response of TB temporal variation at 19 GHz to the instantaneous rainfall. Then, we present the correlation geospatial distribution between rain rate and TB at 19 and 89 GHz, and between rain rate and TB temporal variation at 19 and 89 GHz. We also discuss several factors that affect the correlation between rain rate and TB temporal variation,

Table 1
Mean Footprint Resolution at Each Frequency Used in This Study From SSMIS, AMSR2, and GMI

SSMIS		AMSR2		GMI	
Frequency	Resolution	Frequency	Resolution	Frequency	Resolution
19.4 (V/H)	59 km	18.7 (V/H)	22 km	18.7 (V/H)	15 km
91.7 (V)	14 km	89.0 (V)	5 km	89.0 (V)	7 km

Note. SSMIS = Special Sensor Microwave Imager/Sounder; AMSR2 = Advanced Microwave Scanning Radiometer 2; GMI = Global Precipitation Measurement Microwave Imager.

including the temperature variation, the time differences between raining and nonraining observations, and the soil texture. Finally, the conclusions are summarized in section 5.

2. Data

The TB used in this study is from five instruments, including the Special Sensor Microwave Imager/Sounder (SSMIS) onboard the Defense Meteorological Satellite Program F16, F17, and F18 satellites; the Advanced Microwave Scanning Radiometer 2 (AMSR2) onboard the Global Change Observation Mission-Water satellite; and the Global Precipitation Measurement (GPM) Microwave Imager (GMI) onboard the GPM core satellite.

As a proof-of-concept, we use three channels from each of these five sensors (Table 1). They are 19.4 (V/H) and 91.7 (V) from SSMIS, and 18.7 (V/H) and 89.0 (V) from AMSR2 and GMI. V and H represent the vertical and horizontal polarization, respectively. As shown in Table 1, all these channels have different footprint resolutions (Draper et al., 2015). The slightly different frequency between SSMIS and GMI (AMSR2) also results in different TBs for the same surface background and hydrometeor profile (Yang et al., 2014). Section 3 below demonstrates a method to bring all these frequencies to a similar resolution. We adjust the TBs at similar frequencies from SSMIS and AMSR2 to the GMI frequencies, by the simultaneous conical overpass (SCO) technique (Yang et al., 2011) and a linear regression method. Section 3 presents more details regarding this adjustment. For convenience, we do not distinguish the slight frequency differences among these five sensors from now on, and these channels are referred to as V19, H19, and V89.

The objective of this study is to show that the temporal variation of H19 (primarily the surface emissivity variation signal) is well correlated with the instantaneous precipitation rate. Physically, TB at the horizontal polarization is more sensitive to the land surface characteristics than its counterpart at the vertical polarization, because the horizontal polarized channel is more affected by the polarization of the water particles at/near the surface. Therefore, we choose to show the temporal variation of H19, instead of V19. As a comparison to the surface emissivity variation signal, the temporal variation of V89 (mostly the ice particle scattering signature) is also computed throughout this work. In addition, SSMIS, AMSR2, and GMI have 24, 14, and 13 channels, respectively. We only selected the V19, H19, and V89 channels because 19 and 89 GHz are the lowest and highest commonly available frequency from these five sensors.

The precipitation rate data are from the Multi-Radar/Multi-Sensor System (MRMS), which is at 1-km and 2-min spatial and temporal resolution (Zhang et al., 2016). Collocation between the MRMS precipitation rate and TB is discussed in section 3.

Data used in this study are all from March 2014 to December 2016 over SGP of the United States (95–105°W, 30–45°N). We choose this period of time since observations from all aforementioned five satellites are available. SGP is selected because of the large dynamic emissivity variation due to the precipitation effect (Tian et al., 2015; Turk et al., 2016; You et al., 2014).

The ancillary data used in this study includes Ku-band precipitation radar (KuPR, 13.6 GHz) onboard GPM core satellite (Seto et al., 2013). The precipitation profile observed by KuPR is utilized in the radiative transfer model experiments to distinguish the surface emissivity effect from the hydrometeor effect. Specifically, we select all the KuPR rain rate profiles over the targeted region from March 2014 to December 2016. Then these profiles are averaged according to different surface rain rates (e.g., 1 mm/hr; see Figure 9). In the radiative transfer model simulation, the surface temperature, temperature, and relative humidity profiles are from Modern-Era Retrospective Analysis for Research and Applications, version 2, which are all at 0.625° ×0.5° latitude-longitude spatial resolution. The temporal resolution for the surface temperature and profiles are 1

and 3 hr, respectively. We used the National Ice Center's Interactive Multisensor Snow and Ice Mapping System daily snow cover map at 24 km to screen out the possible snow cover observations. In addition, we also use the gauge-corrected hourly MRMS data for the daily rainfall accumulation computation.

3. Methodology

3.1. Definition of TB Temporal Variation

TB temporal variation (ΔTB) for any channel is defined as

$$\Delta TB = TB_{t_0} - TB_{t_{-1}} \tag{1}$$

$$\Delta t = t_0 - t_{-1} \tag{2}$$

where TB_{t_0} is the current TB associated with precipitation and $TB_{t_{-1}}$ is the preceding TB at the same location without precipitation. A grid box is judged as a precipitating grid box when the TB difference between V19 and V89 is greater than 8 K (Kummerow et al., 2001; Wang et al., 2009). Otherwise, the grid box is considered as a nonprecipitating grid box. By using the 8 K as the threshold value, the probability of detection is 69.24% with the false alarm rate at 6.92% in the targeted region, according to MRMS observations. Δt is the time difference between these two observations. By using these five satellites, Δt varies from several minutes to as long as 24 hr. We discuss later the varying Δt's effect on the correlation between ΔTB and precipitation rate in section 4.4.

This study computes the temporal variation of H19 (hereinafter referred to as $\Delta H19$) and of V89 (hereinafter referred to as $\Delta V89$). We demonstrate later in the section 4.5 from radiative transfer model simulation experiments that the $\Delta H19$ is largely the surface emissivity variation signal due to the precipitation impact, while $\Delta V89$ is primarily the ice scattering signal.

3.2. Aggregate the Higher-Resolution TB

Table 1 shows the mean footprint resolution of SSMIS, AMSR2, and GMI at 19 and 89 GHz (Draper et al., 2015). The 19 GHz of SSMIS has the largest footprint size at 59 km. This study aggregates the finer footprint resolution by simply averaging to roughly match this resolution. Specifically, we average 7 ($59 \times 59/22/22 \approx 7$) pixels of 19 GHz from AMSR2, 16 pixels of 19 GHz from GMI, 18 pixels of 91.7 GHz from SSMIS, 140 pixels of 89 GHz from AMSR2, and 71 pixels of 89 GHz of GMI to approximately match the resolution of 19 GHz of SSMIS (59 km). For the precipitation rate, we simply average the closest 3,481 ($59 \times 59 = 3481$) 1-km MRMS precipitation rate pixels for each TB observation at the closest time.

3.3. Intersatellite Adjustment

After the footprint sizes of these five sensors being brought to a similar resolution, the TBs from SSMIS and AMSR2 for each channel are adjusted to the GMI channels. The GMI channels are taken as the reference channel because AMSR2 and SSMIS are calibrated against GMI (Berg et al., 2016).

The linear relationship between the GMI TB at each channel and the TB from AMSR2 or SSMIS at the similar frequency is assumed, and it takes the following form:

$$TB_{s,c}^{adj} = \beta_0 + \beta_1 \times TB_{s,c}^{obs} \tag{3}$$

where s is from 1 to 4, which stands for sensors of SSMIS onboard F16, F17, and F18, and AMSR2. And c is from 1 to 3, which represents channels of H19, V19, and V89 GHz.

The SCO technique by Yang et al. (2011) is used to obtain the coefficients β_0 and β_1. The idea of SCO technique is that simultaneous measurements at a certain location from two different sensors at similar frequencies should be highly correlated. This study takes the GMI observations as the reference. Two measurements, one from GMI and the other one from any of other four sensors, are called a SCO pair, if the field-of-view location is less than 1 km and the field-of-view time is less than 2 min. These threshold values are chosen by considering the trade-off between the sample size and the SCO pair accuracy.

To obtain enough SCO pairs, we choose the land portion of the region from 70–130°W, 30–50°N. The scatter plots between these SCO pairs for each channel are shown in Figure 1. It is evident that the majority of the SCO pairs are close to the 1-1 line. The coefficients trained by these SCO pairs are listed in Table 2. Most adjusted TBs (~97.0%) deviate less than 2 K from the original TBs.
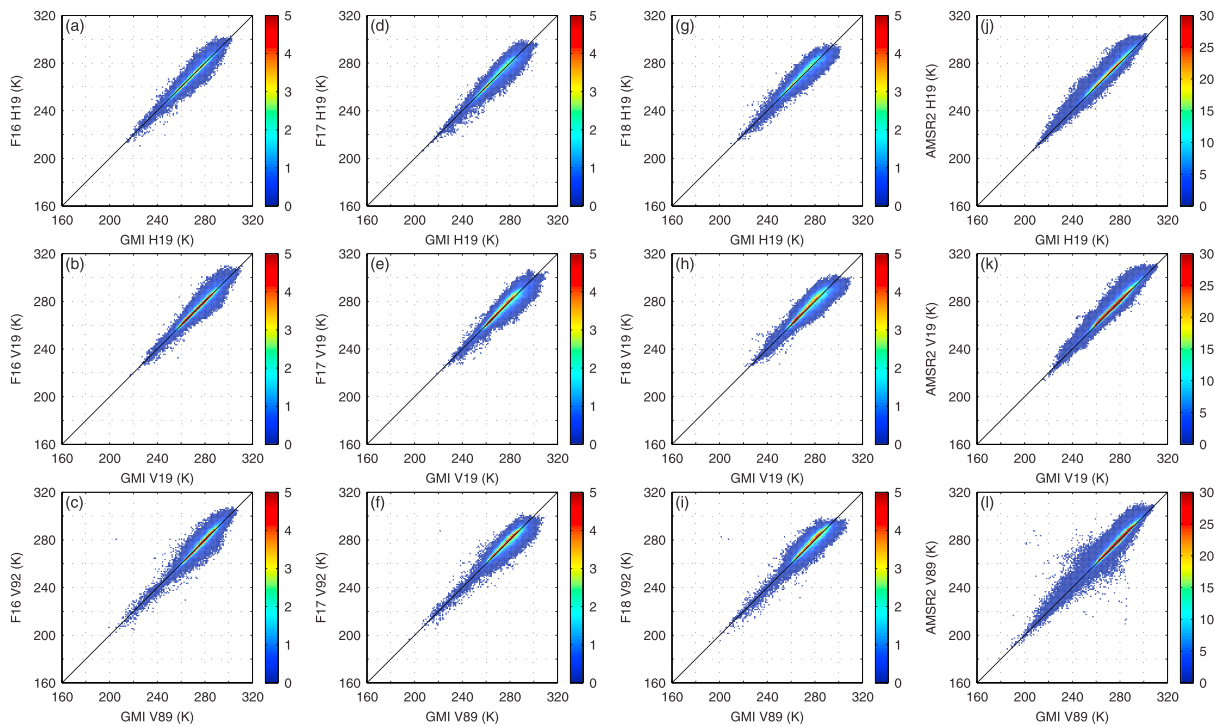
Figure 1. Each column represents the scatter plots of the simultaneous conical overpass pairs between GMI and F16-SSMIS (a–c), between GMI and F17-SSMIS (d–f), between GMI and F18-SSMIS (g–i), and between GMI and AMSR2 (j–l). These simultaneous conical overpass pairs are based on data over the land portion of (70–130°W, 30–50°N) from March 2014 to December 2016, at the nominal resolution of 59 km. GMI = Global Precipitation Measurement Microwave Imager; SSMIS = Special Sensor Microwave Imager/Sounder.

3.4. Definition of the *Same Location*

The purpose of this study is to show that $\Delta H19$ is well correlated with the precipitation rate. Therefore, for a certain location, the number of observations should be high enough to obtain a meaningful temporal variation. To this end, the data are gridded into 0.5° latitude-longitude box. Any pixel in the same grid box is taken as the observation for the same location. We choose the 0.5° resolution because the mean footprint size (59 km) is close to the 0.5° resolution.

Approaches used in this study are very similar to You, Peters-Lidard, et al. (2017). A major difference between this study and You, Peters-Lidard, et al. (2017) is whether to consider the environmental variation from $TB_{t_{-1}}$ to TB_{t_0}. Specifically, this study first uses the same ΔTB definition as You, Peters-Lidard, et al. (2017). Later, we modify ΔTB definition in section 4 to consider the environmental variation (e.g., temperature) from $TB_{t_{-1}}$ to TB_{t_0}, since we are able to more accurately compute the land surface emissivity at low-frequency channels under the nonprecipitating scenarios, compared to at high-frequency channels. In addition, this study grids satellite observations into a 0.5° latitude-longitude box due to the larger footprint size at 19 GHz, compared to the 0.25° latitude-longitude box in You, Peters-Lidard, et al. (2017).

Table 2
Coefficients Used in Equation (3) to Adjust Brightness Temperatures From SSMIS and AMSR2 to GMI Frequency

	F16-SSMIS		F17-SSMIS		F18-SSMIS		AMSR2	
	β_0	β_1	β_0	β_1	β_0	β_1	β_0	β_1
H19	13.94	0.94	12.08	0.96	3.18	0.99	7.83	0.97
V19	12.13	0.96	8.53	0.97	4.89	0.98	8.96	0.96
V89	28.13	0.90	10.10	0.97	12.77	0.95	13.17	0.95

Note. SSMIS = Special Sensor Microwave Imager/Sounder; AMSR2 = Advanced Microwave Scanning Radiometer 2; GMI = Global Precipitation Measurement Microwave Imager.
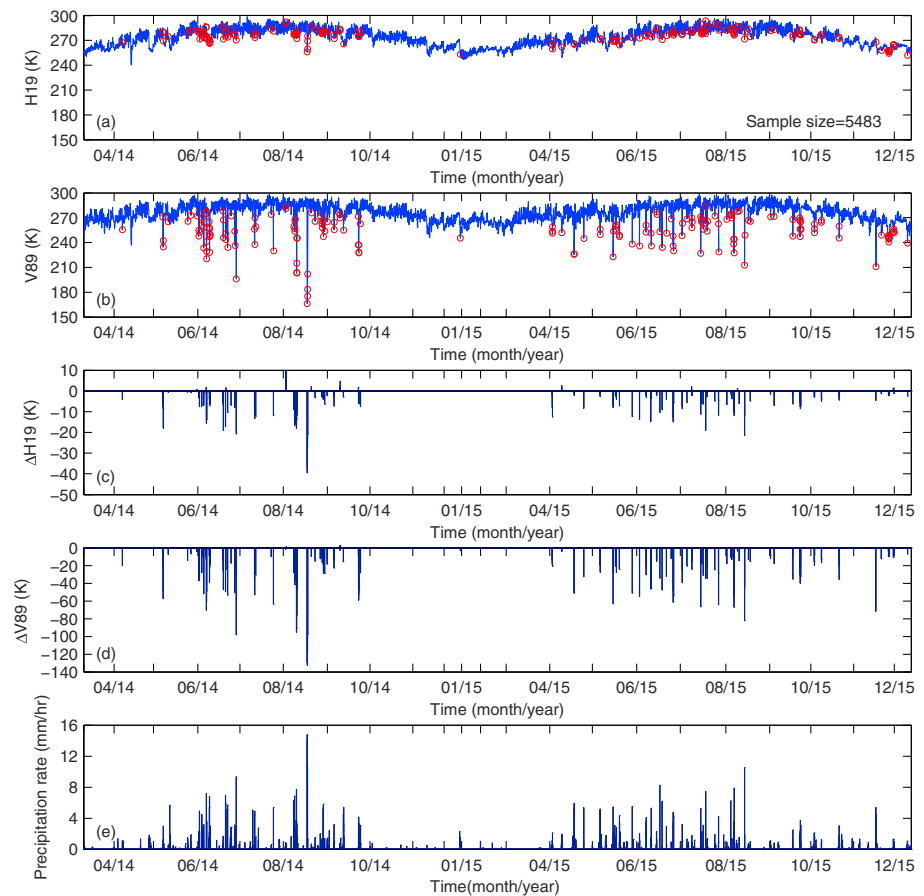
Figure 2. Time series from March 2014 to December 2015 the 0.5° grid box of (100.5–101°W, 41.5–42° N) for (a) H19, (b) V89, (c) ΔH19, (d) ΔV89, and (e) precipitation rate. The red circles in panels (a) and (b) represent the precipitation observations identified by $V19 - V89$ greater than 8 K.

4. Results

4.1. Time Series Analysis

Figure 2 shows the time series of H19 (Figure 2a) and V89 (Figure 2b), and the corresponding precipitation rate (Figure 2e) over the 0.5° grid box of (100.5–101°W, 41.5–42°N). There are 5,483 observations at this location from March 2014 to December 2015. The red circles in Figures 2a and 2b represent the precipitation observations identified by $V19 - V89$ greater than 8 K. The red circles in Figure 2a (observations with precipitation) do not separate themselves from the blue curve. It basically means that the precipitation signal from H19 itself is very weak. In contrast, the TB depression at V89 (Figure 2b) is evident. That is, the observations with red circles correspond well with the precipitation occurrence (the blue bar in the Figure 2e).

The poor correlation between H19 and precipitation rate is immediately evident in the scatter plot (Figure 3a), where the correlation coefficient is only −0.12. The poor correlation (−0.12) is the reason why previous work primarily used the scattering signal at high-frequency channels (e.g., 89 GHz) for the precipitation retrieval over land. In contrast, V89 correlates strongly with precipitation rate with a correlation coefficient of −0.66 (Figure 3c).

Figures 2c and 2d show the time series of ΔH19 and ΔV89 (defined in equation (1). The ΔH19 and ΔV89 are set as 0 for the observations judged as nonprecipitating observations ($V19 - V89 < 8$ K). It is very clear that both ΔH19 (Figure 2c) and ΔV89 (Figure 2d) correspond very well with the precipitation occurrence (Figure 2e).

There are 180 precipitation observations out of 5,483 total observations from March 2014 to December 2015 over this grid box. The vast majority of the ΔH19 associated with precipitation (159 out of 180 records) are less than 0, and the TB depression at ΔH19 can be as large as 40 K. There indeed exists a small portion of the observations (21 out of 180 records) with ΔH19 greater than 0. For the ΔV89, all values are negative. We
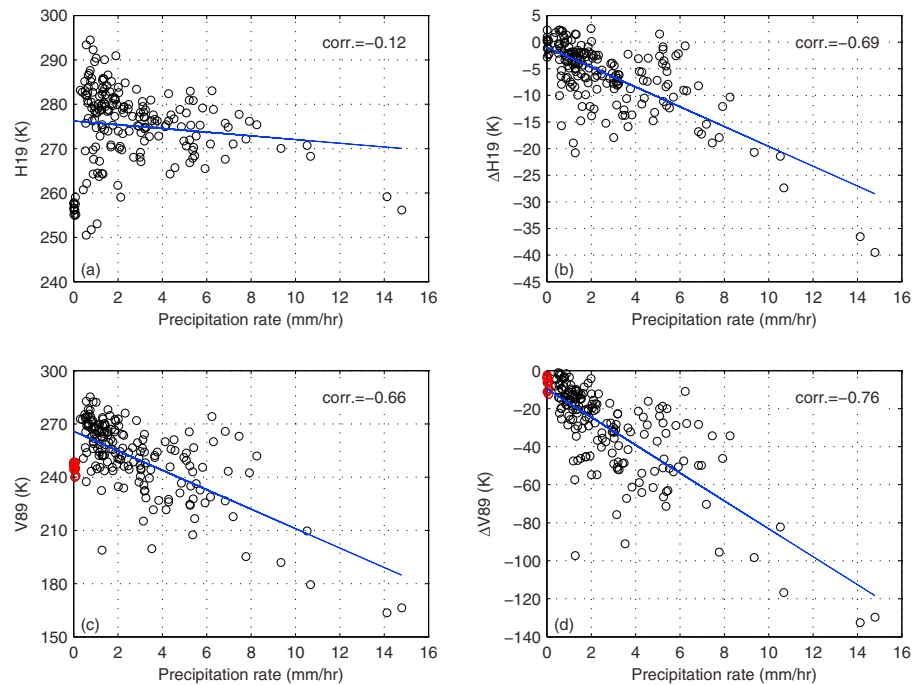
Figure 3. (a) Scatter plot between H19 and precipitation rate over the grid box of (100.5–101°W, 41.5–42°N) from March 2014 to December 2015. (b) Same as (a) except for $\Delta H19$. (c) Same as (a) except for V89. (d) Same as (a) except for $\Delta V89$. The red circles in Figure 3c represent several falsely identified precipitation observations with very cold TB at 89 GHz (∼240 K), which correspond to a very small $\Delta V89$ (close to 0 K) in Figure 3d (red circles). See more discussions in the text.

explain the positive and negative TB values of $\Delta H19$ and $\Delta V89$ by a radiative transfer model simulation in section 4.5.

The much better correlation between $\Delta H19$ and precipitation rate (−0.69), compared with that between H19 itself and precipitation rate (−0.12), is obvious in Figure 3 (cf. Figures 3b and 3a). It is worth noting that the correlation between $\Delta H19$ and precipitation rate (−0.69; Figure 3b) is slightly worse than that between $\Delta V89$ and precipitation rate (−0.76; Figure 3d). In the following sections, we show that the highly variable time difference (Δt) is largely responsible for the worse performance of $\Delta H19$. Another possible reason is that the signal magnitude of $\Delta H19$ is weaker than that of $\Delta V89$. The correlation between $\Delta V89$ and precipitation rate (−0.76) is also better than that between V89 and precipitation rate (−0.66; Figure 3c) due to the mitigation of cold surface contamination. We use the daily Ice Mapping System snow cover map to filter out possible snow-covered observations. However, there may still exist some observations associated with snow cover on the ground due to the mismatch between the daily snow cover map and the instantaneous satellite observations. Specifically, the red circles associated with cold V89 at ∼240 K in Figure 3c represent the falsely identified precipitating observations. The influence of the falsely identified precipitation observations due to the cold surface is largely reduced when using $\Delta V89$, because the $\Delta V89$ of these falsely identified observations are close to 0 (Figure 3d). More discussions regarding the mitigation of the surface contamination at 89 GHz are contained in You, Peters-Lidard, et al. (2017).

In summary, it is demonstrated that $\Delta H19$ is well correlated with the precipitation rate, while H19 itself has very weak correlation with the precipitation rate.

4.2. Correlation Over the SGP
The correlation between $\Delta H19$ and precipitation rate (Figure 4a), between H19 and precipitation rate (Figure 4b), between $\Delta V89$ and precipitation rate (Figure 4d), and between V89 and precipitation rate (Figure 4e), are computed over SGP. The precipitation occurrence number, judged by the scattering index method ($SI = V19 − V89$), varies from 40 to 404 in different grid boxes.

As discussed above, it is clear that $\Delta H19$ is much better correlated with the precipitation rate than H19 itself (cf. Figures 4a and 4b). The majority of the correlation coefficients (64.8%) between $\Delta H19$ and precipitation
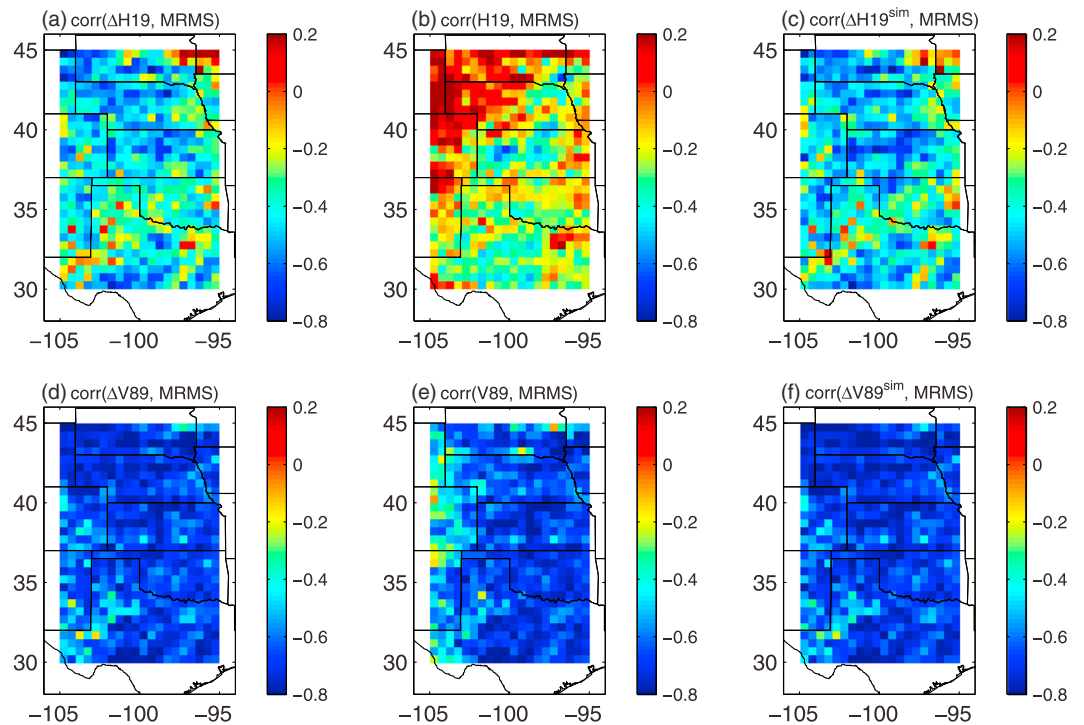
Figure 4. (a) Correlation coefficients between $\Delta H19$ and Multi-Radar/Multi-Sensor System (MRMS) precipitation rate. (b) Correlation coefficients between H19 and MRMS precipitation rate. (c) Correlation coefficients between $\Delta H19^{sim}$ and MRMS precipitation rate. (d) Correlation coefficients between $\Delta V89$ and MRMS precipitation rate. (e) Correlation coefficients between V89 and MRMS precipitation rate. (f) Correlation coefficients between $\Delta V89^{sim}$ and MRMS precipitation rate.

rate are negative (less than -0.4). As shown in the case study, most $\Delta H19$ decreases due to the impact of precipitation. Mathematically, this explains why $\Delta H19$ and precipitation rate is negatively correlated. Physically, precipitation usually increases the soil moisture and therefore leads to a depression in emissivity which results in a TB depression. On the other hand, out of the 600 correlation coefficients, there are 14 positive ones. These positive correlation coefficients caused by (1) the combined effect of surface emissivity variation and hydrometeors emission/scatter in the air, which we explain in detail in section 4.5; and (2) cold surfaces misidentified as precipitation. The false positive correlation between H19 itself and precipitation rate is especially obvious in the top left corner of Figure 4b. These false positive correlations are generally caused by cold surface contamination (e.g., snow on the ground).

Over SGP, the vast majority of the correlation coefficients between $\Delta V89$ and precipitation rate (Figure 4d) are less than -0.7. Obviously, the scattering signature is better correlated with the precipitation than the surface emissivity variation signal. In the following sections, we demonstrate that the correlation between $\Delta H19$ and precipitation rate is highly dependent on the Δt variation, while the correlation between $\Delta V89$ and precipitation rate is relatively independent from the Δt variation. Even though five satellite observations are exploited in this study, the Δt is still highly variable, which can change from several minutes to more than 12 hr. The highly variable Δt has a larger negative impact on the correlation between $\Delta H19$ and precipitation rate than that between $\Delta V89$ and precipitation rate, because $\Delta H19$ is more sensitive to the surface characteristics than $\Delta V89$.

Another interesting phenomenon is that $\Delta V89$ is better correlated with the precipitation rate than V89 itself, which is particularly evident over west of 103°W. As mentioned previously, in these regions, the $\Delta V89$ can more effectively mitigate the surface contamination, especially under the light precipitation scenario (You, Peters-Lidard, et al., 2017).

4.3. Temperature Variation Influence

In section 3, we define the ΔTB as $TB_{t_0} - TB_{t_{-1}}$. In this definition, we do not consider the temperature (surface temperature and temperature profile) variation from t_{-1} to t_0. In other words, it explicitly assumes that the
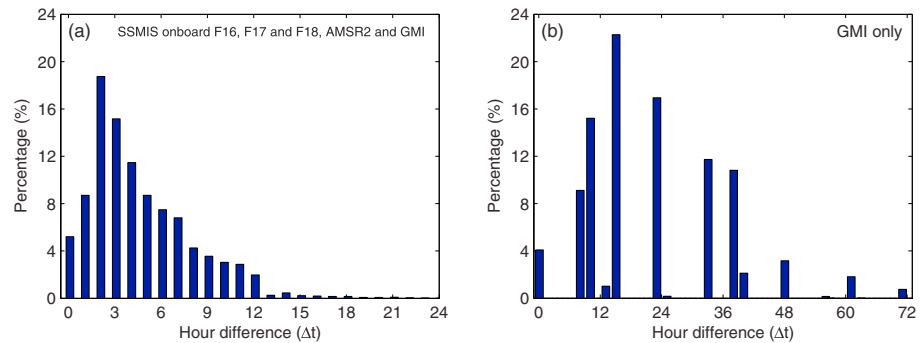
Figure 5. (a) Histogram of the time difference (Δt in equation (2) when using five sensors, including SSMIS onboard F16, F17, and F18; AMSR2; and GMI. (b) Same as (a) except when using GMI only. SSMIS = Special Sensor Microwave Imager/Sounder; AMSR2 = Advanced Microwave Scanning Radiometer 2; GMI = Global Precipitation Measurement Microwave Imager.

temperature information at time t_0 is the same as that at time t_{-1}. This assumption may lead to an error in the ΔTB estimate when the temperature varies from t_{-1} to t_0, especially when Δt is large (e.g., > 12 hr) between these two observations.

To consider the temperature variation, ΔTB may be calculated in the following way:

$$\Delta TB = TB_{t_0} - TB_{t_0}^{sim} \tag{4}$$

where TB_{t_0} is still the observed TB under the precipitating conditions. $TB_{t_0}^{sim}$ is the simulated TB at t_0 by using the emissivity calculated at t_{-1} (under the nonprecipitating condition). Specifically, the emissivity at 19 and 89 GHz is calculated at t_{-1} under the nonprecipitating condition by using the temperature information at t_{-1}. Then the emissivity values at 19 and 89 GHz are used to calculate $TB_{t_0}^{sim}$ by using the temperature information at t_0. By doing so, the surface temperature variation from t_{-1} to t_0 is taken into consideration. From now on, ΔTB computed in equation (4) for H19 and V89 is referred as to $\Delta H19^{sim}$ and $\Delta V89^{sim}$, respectively.

A radiative transfer model (G. Liu, 1998) computes the emissivity under the nonprecipitating conditions. This model calculates the TBs at different microwave frequencies through the discrete ordinate method at varying stream numbers. In the current simulation, the stream number is set as 4. The water vapor absorptions from both line and continuum contributions are considered in this model. The temperature information used in the radiative transfer model calculation is from Modern-Era Retrospective Analysis for Research and Applications, version 2.

By considering the temperature variation effect, it is noted that the correlation between $\Delta H19^{sim}$ and precipitation rate is improved (cf. Figures 4a and 4c). For example, the overall mean correlation coefficient in the targeted region from ΔTB_{19} is −0.40, while it increases to −0.47 using $\Delta H19^{sim}$. Improvement has also been made for the V89 channel, but to a lesser degree (cf. Figures 4d and 4f).

4.4. Influence of Varying Time Difference (Δt)

The objective of this study is to show the temporal variation of TB at 19 GHz ($\Delta H19$) is well correlated with the precipitation rate. Ideally, observations from a satellite constellation with the same configuration or a geostationary microwave radiometer would be most suitable. However, such observations currently are not available or even planned. Therefore, we exploit observations from five low Earth orbit satellites in the GPM constellation. By doing this, the Δt defined in equation (2) is highly variable. This section demonstrates the effect of variable Δt on the correlation between $\Delta H19$ and precipitation rate, and between $\Delta V89$ and precipitation rate.

Figure 5 shows the histogram of the time differences (i.e., Δt). By using five satellite observations, about 99.3% of the Δts are less than 12 hr. In contrast, about 78.8% of the Δts are greater than 12 hr when only GMI observations are used. To show the variable Δt effect, we calculate the correlation between $\Delta H19$ and precipitation rate, and between $\Delta V89$ and precipitation rate, corresponding to different Δts (Figure 6). The correlation coefficients between $\Delta H19$ and precipitation rate decrease quickly from −0.5 with Δt at 2 hr to −0.21 with Δt at 24 hr. This result implies that with increasing time differences between t_{-1} and t_0, it is more likely that the surface conditions (e.g., soil moisture variation and precipitation in between these two observations) have changed. Therefore, $\Delta H19$ more likely contains other information besides the current precipitation effect.
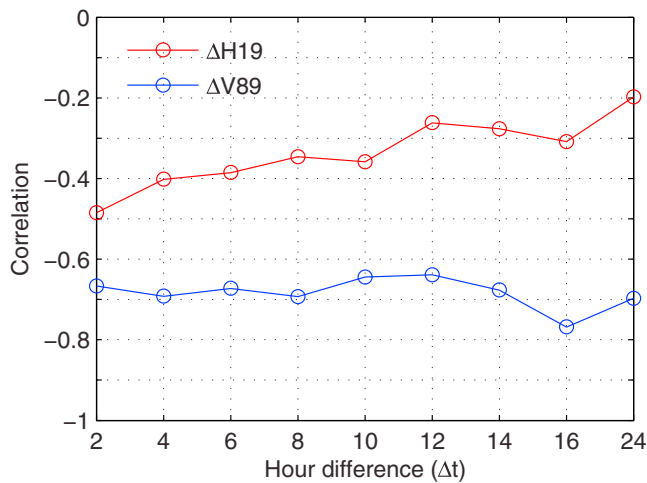
Figure 6. Correlation between $\Delta H19$ and precipitation rate, and between $\Delta V89$ and precipitation rate, under different Δt conditions. The time differences (Δt) are binned into smaller intervals as follows: 0–2, 2–4, …, 14–16, and 16–24 hr.

In contrast, the correlation between $\Delta V89$ and precipitation rate remains at about -0.7 (blue curve in Figure 6), regardless of the Δt variation. The relative independence of $\Delta V89$ indicates that V89 is less affected by the surface characteristics variation in this region, compared with H19. Therefore, using single satellite observations to compute $\Delta V89$ may be sufficient in this region.

Figure 6 shows that correlations between $\Delta H19$ and the precipitation rates decrease as Δt increases. To further understand this phenomenon, we compute the number of precipitation events (Figure 7a), and the percentage of the current precipitation being the only precipitation (Figure 7b), corresponding to different Δt intervals, from 0–1, 1–2, …, 11–12 hr.

As expected, Figure 7a shows that there are more precipitation events with a larger Δt. For example, on average, there are only 1.01 precipitation events when Δt is 1 hr. In contrast, there are 2.78 precipitation events when Δt is 12 hr. When the precipitation-free scene at t_{-1} is less than 1 hr apart from the current precipitating scene at t_0, 99.12% of the time the current precipitation is the only precipitation event in the time period of Δt (Figure 7b). When Δt increases to 12 hr, the percentage decreases to 43.75%, meaning that 56.25% of the time there are other precipitation events in the time period of 12 hr. When there are other precipitation events occurring in the time period of Δt, $\Delta H19$ not only reflects impact of the current precipitation event, it may also include the impact from other precipitating events in between Δt. Therefore, the correlation between $\Delta H19$ and the current precipitation rate becomes weaker as Δt increases.

Since $\Delta H19$ may reflect the precipitation accumulation in the time period of Δt, it is possible to estimate the precipitation accumulation from $\Delta H19$. In fact, previous studies estimated the precipitation accumulation (e.g., daily accumulation) from emissivity at low frequencies channels (You et al., 2014) or from soil moisture (Brocca et al., 2014). However, further analysis shows that the correlation between $\Delta H19$ and the precipitation accumulation in the time period of Δt is not necessarily stronger than that between $\Delta H19$ and the instantaneous precipitation, because the correlation between $\Delta H19$ and the precipitation accumulation is dependent on the time interval in which the precipitation accumulation is computed. More research is necessary to pinpoint the optimal precipitation accumulation time interval.

4.5. Surface Emissivity Effect Versus Hydrometeor Effect

Under precipitating conditions, it is impossible to know the exact value of the emissivity because TB reflects the combined effect from both the surface background emission and scattering/emission from the hydrometeors aloft. To show the possible emissivity variability over the targeted region, we adopt the method in Ferraro et al. (2013). That is, we show the precipitation-free emissivities at H19 and V89, and TBs for the same channels, corresponding to different previous 1-day precipitation accumulation amounts. We can reasonably assume that the emissivity variation under the precipitating conditions resembles the emissivity variation under the precipitation-free scenes, but with different 1-day precipitation accumulation amounts.
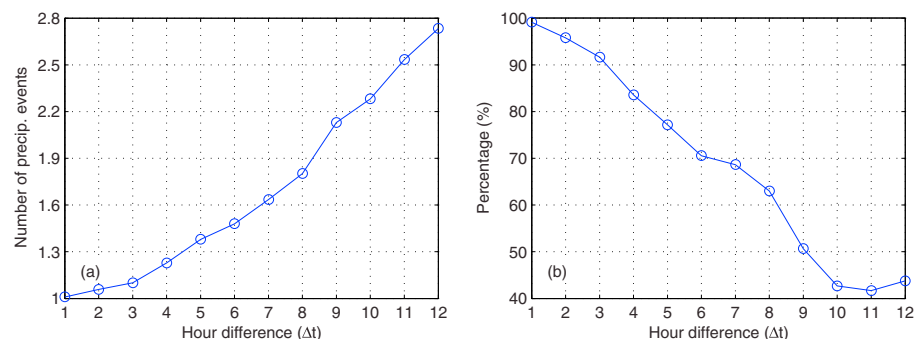

Figure 7. (a) Number of precipitation events in the time period of Δt (between t_{-1} and t_0). (b) Percentage of the precipitation event at t_0 being the only precipitation event in the time period of Δt.

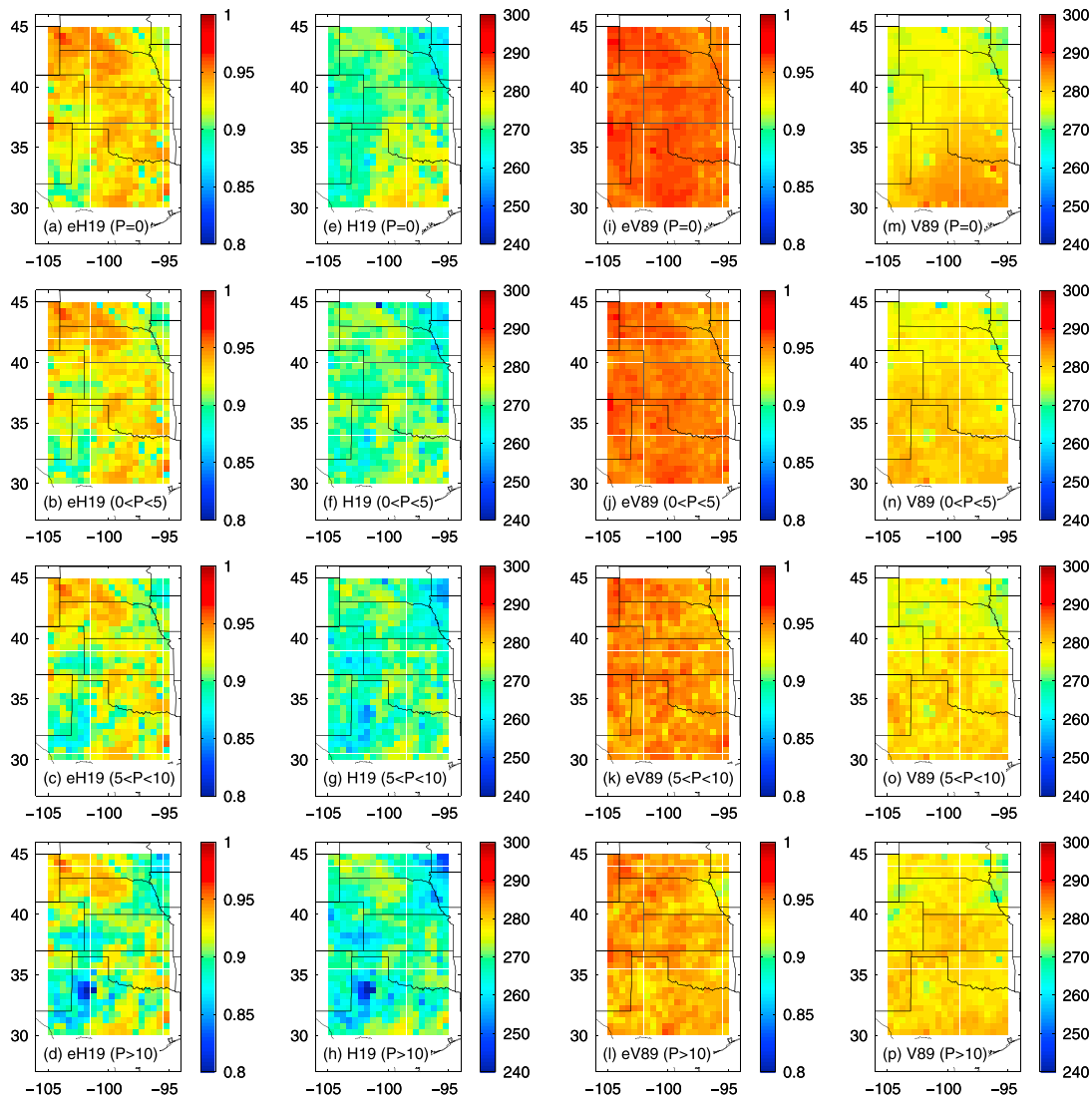**Figure 8.** Corresponding to different previous 1-day precipitation amounts (represented by *P*) at *P* = 0, 0 < *P* < 5, 5 < *P* < 10, and *P* > 10 mm: (a–d) mean emissivity at H19 under the precipitation-free scene; (e–h) mean H19 under the precipitation-free scene; (i–l) mean emissivity at V89 under the precipitation-free scene; (m–p) mean V89 under the precipitation-free scene. The 1-day precipitation amount is calculated from gauge-corrected hourly Multi-Radar/Multi-Sensor System data.

Figure 8a shows that the emissivity for H19 can drop as much as 0.05 from 0.95 to 0.90, or even 0.1 in some areas, corresponding to 10-mm 1-day accumulation precipitation (cf. Figures 8a and 8d). Correspondingly, H19 TB can drop as much as 20 K (cf. Figures 8e and 8h). In contrast, the emissivity at V89 and V89 itself have a much smaller variation magnitude, corresponding to the same amount previous 1-day precipitation accumulation (cf. Figures 8i and 8l, and Figures 8m and 8p). This study shows the concept of using surface emissivity temporal variation signal at the 19 GHz due to the precipitation impact.

As mentioned previously, it is very difficult to separate the surface emissivity contribution from the hydrometeor contribution to the satellite-observed TB, under the precipitating conditions. To disentangle the surface emissivity from hydrometeor effects and better understand the effect from each of them, we conduct following radiative transfer simulation experiments: (1) Simulate TB at H19 and V89 with the surface precipitation rate increasing from 0 to 20 mm/hr, corresponding to the surface emissivity at 0.8, 0.9, 0.95, and 1.0. By doing this, we can determine the hydrometeor effect. (2) Simulate TB at H19 and V89 with the surface emissivity decreasing from 1.0 to 0.8, corresponding to 0, 0.5, and 5 mm/hr precipitation rate. By doing this, we can determine the surface emissivity effect. The radiative transfer model, developed by G. Liu (1998), is used for the
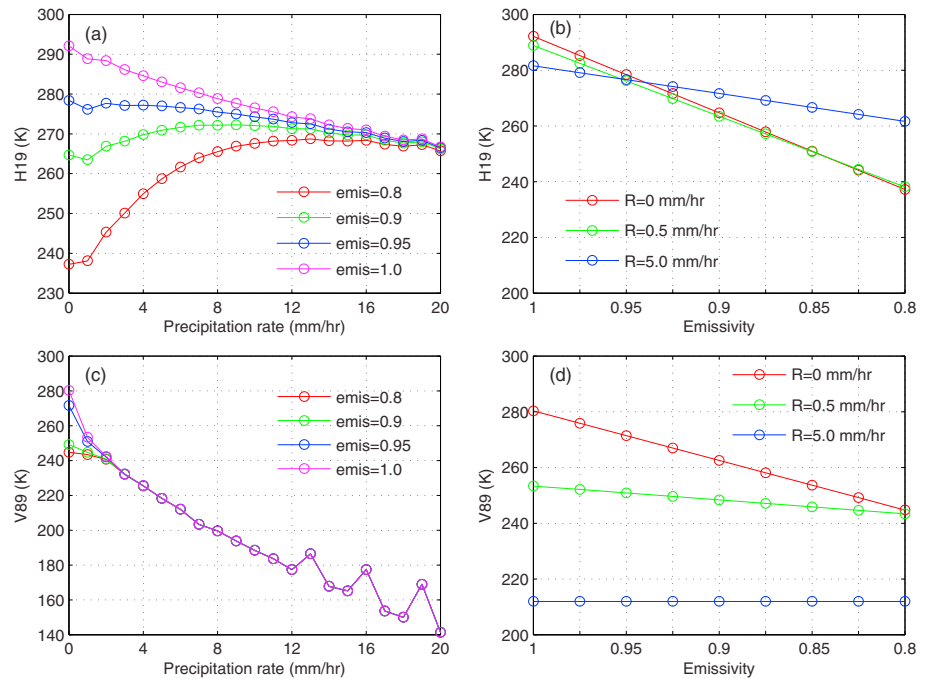
Figure 9. (a) Simulated brightness temperature (TB) at H19 when precipitation rate increases from 0 to 20 mm/hr, corresponding to surface emissivity at 0.8, 0.9, 0.95, and 1.0. (b) Simulated TB at H19 when surface emissivity decreases from 1.0 to 0.8, corresponding to precipitation rate at 0, 0.5, and 5 mm/hr. (c) Simulated TB at V89 when precipitation rate increases from 0 to 20 mm/hr, corresponding to surface emissivity at 0.8, 0.9, 0.95, and 1.0. (d) Simulated TB at V89 when surface emissivity decreases from 1.0 to 0.8, corresponding to precipitation rate at 0, 0.5, and 5 mm/hr.

aforementioned experiments. Additionally, for simplicity the particles above (below) the freezing level height are considered as ice (liquid) particles, and no mixed phase particles are considered in the simulation.

It is found that H19 decreases about 25 K from 292 to 267 K (Figure 9a, magenta curve), and about 12 K from 278 to 266 K (Figure 9a, blue curve), with the precipitation rate increasing from 0 to 20 mm/hr, corresponding to the emissivity at 1.0 and 0.95, respectively. On the contrary, H19 increases from 237 to 266 K (Figure 9a, red curve) when the precipitation rate increases from 0 to 20 mm/hr, with emissivity at 0.8. This partially explains why $\Delta H19$ is positively correlated with the precipitation rate. The green curve in Figure 9a shows that H19 increases slightly when the precipitation rate increases from 0 to 8 mm/hr, then decreases slightly when the precipitation rate increases from 8 to 20 mm/hr. It is clear that TB at H19 can either increase or decrease due to the hydrometeor effect, depending on the different surface emissivity situations. The largest possible TB depression at H19 caused by hydrometeors is probably less than 12 K, since the mean emissivity at H19 under dry condition is less than 0.95 in the targeted region (Figure 8a).

Figure 9b demonstrates that H19 can decrease as much as 55 K from about 292 K to about 237 K under the nonprecipitating condition (Figure 9b, red curve) when emissivity decreases from 1.0 to 0.8. Similar magnitudes of the TB depression are observed under the light precipitation scenario (Figure 9b, green curve). Under heavier precipitation (Figure 9b, blue curve), H19 can decrease about 20 K.

Compared with the mixed hydrometeor effect on H19, the surface emissivity depression caused by precipitation can only lead to a TB depression at H19, and the magnitude of the depression can be as large as 55 K. Our results show that the vast majority of $\Delta H19$s are negative, and its magnitude can be as large as 40 K. From the radiative transfer model simulation experiments, we conclude that the surface emissivity depression plays a larger role in the vast majority of negative $\Delta H19$s. That is, the signal from $\Delta H19$ is largely from the surface emissivity depression, and the hydrometeor scattering/emission signal contributes less to $\Delta H19$.

Compared with the surface emissivity variation signal, it is very clear that the hydrometeor scattering signal is responsible for the TB variation at V89. Figure 9c shows that TB at V89 does not vary when the precipitation rate is larger than 2 mm/hr, regardless of the surface emissivity values. Similar results can be found in Figure 9d.

Table 3
Correlation Between MRMS Precipitation Rate (PR) and $\Delta H19^{sim}$, Between PR and $\Delta V89^{sim}$, Between PR and $\Delta H19$, and Between PR and $\Delta V89$, Conditioned on the Soil Texture Type, Over the Southern Great Plains of the United States (95–105°W, 30–45°N) From March 2014 to December 2016

Soil texture type	Corr(PR, $\Delta H19^{sim}$)	Corr(PR, $\Delta V89^{sim}$)	Corr(PR, $\Delta H19$)	Corr(PR, $\Delta V89$)
Sand	−0.48	−0.67	−0.47	−0.66
Sandy loam	−0.40	−0.68	−0.39	−0.66
Silt loam	−0.45	−0.69	−0.43	−0.67
Loam	−0.45	−0.67	−0.42	−0.65
Silty clay loam	−0.37	−0.68	−0.34	−0.67
Clay loam	−0.38	−0.68	−0.32	−0.65
Clay	−0.41	−0.68	−0.40	−0.65

Note. MRMS = Multi-Radar/Multi-Sensor System.

For example, V89 only decreases about 10 K when emissivity decreases from 1.0 to 0.8, with the precipitation rate at 0.5 mm/hr.

To summarize, the radiative transfer model simulation shows that the $\Delta H19$ largely reflects the surface emissivity variation. In contrast, the hydrometeor scattering signal is responsible for the TB depression of $\Delta V89$. This channel is surface blind with the precipitation rates greater than 2 mm/hr.

4.6. Soil Texture Dependence

The previous section shows that the signal from $\Delta H19$ is essentially the surface emissivity variation due to the precipitation impacts. A key factor affecting the surface emissivity variation is the soil texture (e.g., content and structure) . Therefore, this section explores the possible influence of the soil texture on the correlation between $\Delta H19$ and precipitation rate. As a comparison, the soil texture influence on the correlation between $\Delta V89$ and precipitation rate is also investigated.

Of the 16 soil texture types present in the hybrid State Soil Geographic/Food and Agriculture Organization soil texture data set provided by the National Center for Atmospheric Research for the Noah land surface model (Miller & White, 1998; Reynolds et al., 2000), 10 types are represented in the targeted region. They are sand (63), loamy sand (5), sandy loam (103), silt loam (142), loam (129), silty clay loam (48), clay loam (58), silty clay (8), clay (41), and other (3). The number in the parenthesis following the soil texture types is the 0.5° grid box number for each class. For example, the soil type is sand in 63 grid boxes, out of 600 grid boxes in the whole targeted region. The following calculation omits the classes of loamy sand, silty clay and other, due to the limited sample size.

The correlation between $\Delta H19^{sim}$ and precipitation rate (Figure 4c) is averaged for each soil texture type. Similar computation is performed for the correlation between $\Delta V89^{sim}$ and precipitation rate (Figure 4f). Results are listed in Table 3. The correlations between $\Delta H19^{sim}$ and precipitation rate have a general decreasing trend from the sand soil to the clay soil. We hypothesize that the better correlation from the sand soil is due to the quicker response of the sand to the instantaneous precipitation impact, compared with the clay soil. Another possible reason is that precipitation events in-between Δt (other than the current precipitation event) may have a smaller impact on the sandy soils, because water drains away faster through the sandy soils, compared with clay soils. As shown in Figure 7a, when the Δt is larger than 1 hr, precipitation events other than the current precipitation event likely occur. More work is necessary to fully understand the underlying physical reason for this behavior.

In contrast, the soil texture type has almost no influence on the correlation between $\Delta V89^{sim}$ and precipitation rate, as indicated by the almost constant correlation coefficients ($\sim$ −0.68) between them. It is worth mentioning that using the correlation coefficients between $\Delta H19$ and precipitation rate (Figure 4a), and between $\Delta V89$ and precipitation rate (Figure 4d) generates very similar results (see last two columns of Table 3).

4.7. Precipitation Retrieval Over the SGP

The ability of $\Delta H19$ to retrieve precipitation is investigated by using the independent data in 2016. As a proof-of-concept, a simple linear regression line is fitted between the $\Delta H19$ and precipitation rate using the training data set from 2014 to 2015 in each 0.5 grid box. As comparisons, similar procedures are applied to
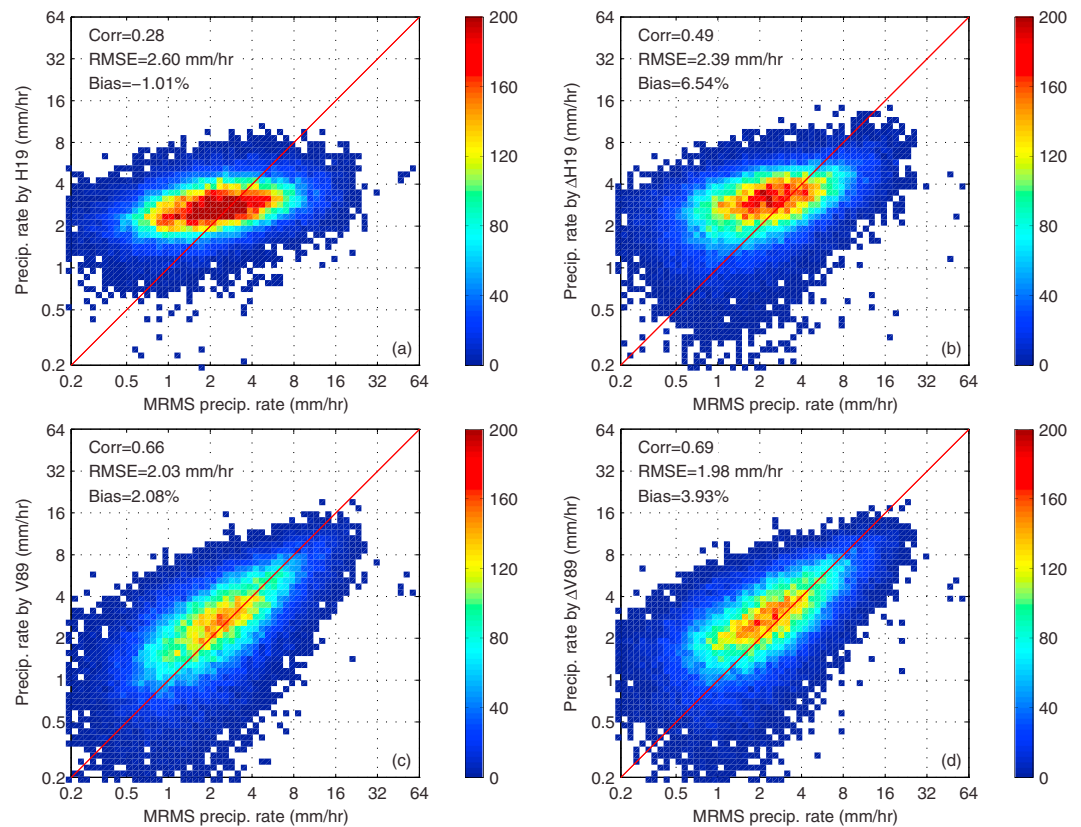
Figure 10. Scatter plots between surface radar observed precipitation rate (reference) and (a) retrieved precipitation rate from H19; (b) retrieved precipitation rate from ΔH19; (c) retrieved precipitation rate from V89; and (d) retrieved precipitation rate from ΔV89. RMS = root-mean-square; MRMS = Multi-Radar/Multi-Sensor System.

H19, V89 and ΔV89 to retrieve the precipitation rate. Then the fitted regression line in each grid box is used to retrieve the precipitation rate in 2016, where the MRMS precipitation rate is taken as the reference.

Figure 10 shows the overall retrieval results over SGP. The retrieved precipitation rate from ΔH19 has a correlation of 0.49 with MRMS. Root-mean-square error is about 2.39 mm/hr, and the bias is 6.54% (Figure 10b). The retrieval result from H19 itself (Figure 10a) performs noticeably worse, as indicated by a much smaller correlation of 0.28. It is noted that the bias from H19 (−1.01%) is smaller than that from ΔH19 (6.54%), because the larger positive bias at the lower end of the precipitation rate and the larger negative bias at the higher end of the precipitation rate are canceled out each other in the retrieval result of H19 (Figure 10a).

The retrieval results from V89 (Figure 10c) and ΔV89 (Figure 10d) are obviously better, compared with ΔH19. The highly variable Δt likely affects the ΔH19's performance, because ΔH19 is much more sensitive to the surface characteristics variation than ΔV89. Previous analysis shows that the magnitude of the correlation between ΔH19 and precipitation rate decreases quickly along with the Δt increase. This again suggests that a denser low earth orbit microwave constellation or a geostationary microwave radiometer could help to improve the performance of ΔH19 for the precipitation retrieval. In addition, we show that the correlation between ΔH19 and precipitation rate is dependent on the soil texture type, which has little influence on the correlation between ΔV89 and precipitation rate.

5. Conclusions and Discussions

This study extends our previous work (You, Peters-Lidard, et al., 2017) on temporal changes in high-frequency TBs to demonstrate the potential value of low-frequency channels to improve precipitation rate retrievals over land. For this study, we use 3-year (2014–2016) observations over SGP from surface radar measured precipitation rate and five satellites observed TBs, including SSMIS onboard F16, F17, and F18; AMSR2; and GMI.

Over the whole study region, $\Delta H19$ and precipitation rate is well correlated with the majority of the correlation coefficients less than −0.4. The correlation can be further improved by considering the temperature temporal variation through the radiative transfer model simulation. It is also noted that the correlation from V89 or $\Delta V89$ is stronger than that from $\Delta H19$. The relatively worse performance of the $\Delta H19$ is due to this signal being more sensitive to the surface characteristics than $\Delta V89$. Even with observations from five sensors, Δt varies from several minutes to more than 12 hr. It is shown that the correlation between $\Delta H19$ and precipitation rate substantially weakens as Δt increases. We suggest that the observations from a denser low Earth orbit microwave constellation or a hypothetical geostationary microwave radiometer can improve the correlation between $\Delta H19$ and precipitation rate due to its high temporal resolution.

We further analyze the signal source of the $\Delta H19$. Results show that the surface emissivity depression caused by the precipitation is largely responsible for the $\Delta H19$ variation, while the hydrometeor scattering/emission effect contributes much less to the $\Delta H19$ behavior. In contrast, the TB at 89 GHz is surface blind under the moderate and heavy precipitation scenarios (e.g., > 2 mm/hr in Figure 9c), and it is the hydrometeor scattering effect that results in the TB depression at 89 GHz, which is well documented in the literature (Ferraro & Marks, 1995; McCollum & Ferraro, 2003; Wang et al., 2009; You et al., 2015, 2016).

Further analysis shows that the correlation between $\Delta H19$ and precipitation rate varies over different soil texture types, with the largest correlation for the sand soil type. In contrast, soil texture has almost no influence on the correlation between $\Delta V89$ and precipitation rate.

As a proof-of-concept, a linear regression precipitation retrieval is performed over SGP by using the independent data in 2016. On average, the retrieved precipitation rate from $\Delta H19$ has a correlation of 0.49, a root-mean-square error of 2.39 mm/hr and a bias of 6.54% , compared with the surface radar observations. These statistics are much better than those from H19 itself. However, it is noted that performance from $\Delta V89$ is better than that from $\Delta H19$, partially due to the larger negative influence to $\Delta H19$ from the highly variable time difference (Δt) between two observations. As a proof-of-concept, this study only uses five satellites to derive the TB temporal variation. In fact, several other currently operational radiometers carry the low-frequency channels at ~19 GHz, including Advanced Microwave Sounding Unit-A, Advanced Technology Microwave Sounder, WindSat, and FengYun-3 Microwave Radiometer Imager. By using all observations from these radiometers (10+), it could significantly increase the temporal resolution, and therefore, the performance of $\Delta H19$ is expected to improve greatly. By doing so, the previous overpasses of all used sensors (five in the current study) need to be processed and stored, which can take longer time compared with the retrieval algorithm for a single sensor.

Finally, it is not our purpose to claim that the surface emissivity signal from $\Delta H19$ is stronger than the scattering signal from either $\Delta V89$ or V89 itself. In fact, results in Figure 10 show that the scattering signal over the targeted region is stronger than the surface emissivity variation signal from $\Delta H19$. The primary objective of this study is to show that $\Delta H19$ largely reflects the surface emissivity variation due to the precipitation impact. Therefore, it provides an independent signal source for precipitation retrieval, which may complement the scattering signal from high-frequency channels under certain situations. For example, in the warm rain systems there are few or no ice particles. Therefore, the scattering signal at high-frequency channels is rather weak, which leads to a poor precipitation retrieval result for algorithms solely dependent on the ice scattering signature (C. Liu & Zipser, 2009; Sohn et al., 2013; You & Liu, 2012). In addition, Hamada et al. (2015) showed that a large scattering signal does not necessarily indicate heavy precipitation. Our study shows that it is possible to use the signal from the surface emissivity variation, as reflected in TB temporal variation derived from low-frequency channels, to measure the instantaneous precipitation rate, which currently is not considered in the instantaneous precipitation retrieval. Future work seeks to combine these two signal sources (scattering from the hydrometeors aloft and surface emission variation due to the precipitation) to achieve an optimal precipitation retrieval performance.

References

Aonashi, K., Awaka, J., Hirose, M., Kozu, T., Kubota, T., Liu, G., et al. (2009). GSMaP passive microwave precipitation retrieval algorithm: Algorithm description and validation. *Journal of the Meteorological Society of Japan*, *87*, 119–136.

Berg, W., Bilanow, S., Chen, R., Datta, S., Draper, D., Ebrahimi, H., et al. (2016). Intercalibration of the GPM microwave radiometer constellation. *Journal of Atmospheric and Oceanic Technology*, *33*(12), 2639–2654.

Birman, C., Karbou, F., & Mahfouf, J.-F. (2015). Daily rainfall detection and estimation over land using microwave surface emissivities. *Journal of Applied Meteorology and Climatology*, *54*(4), 880–895.

Brocca, L., Ciabatta, L., Massari, C., Moramarco, T., Hahn, S., Hasenauer, S., et al. (2014). Soil as a natural rain gauge: Estimating global rainfall from satellite soil moisture data. *Journal of Geophysical Research: Atmospheres*, *119*, 5128–5141. https://doi.org/10.1002/2014JD021489

Crow, W. T., Huffman, G. J., Bindlish, R., & Jackson, T. J. (2009). Improving satellite-based rainfall accumulation estimates using spaceborne surface soil moisture retrievals. *Journal of Hydrometeorology*, *10*(1), 199–212.

Draper, D. W., Newell, D., Wentz, F. J., Krimchansky, S., & Skofronick-Jackson, G. M. (2015). The Global Precipitation Measurement (GPM) Microwave Imager (GMI): Instrument overview and early on-orbit performance. *IEEE Journal of Selected Topics in Applied Earth Observations and Remote Sensing*, *8*, 3452–3462.

Ferraro, R. R., Grody, N. C., & Marks, G. F. (1994). Effects of surface conditions on rain identification using the DMSP-SSM/I. *Remote Sensing Reviews*, *11*(1–4), 195–209.

Ferraro, R. R., & Marks, G. F. (1995). The development of SSM/I rain-rate retrieval algorithms using ground-based radar measurements. *Journal of Atmospheric and Oceanic Technology*, *12*(4), 755–770.

Ferraro, R. R., Peters-Lidard, C. D., Hernandez, C., Turk, F. J., Aires, F., Prigent, C., et al. (2013). An evaluation of microwave land surface emissivities over the continental United States to benefit GPM-era precipitation algorithms. *IEEE Transactions on Geoscience and Remote Sensing*, *51*(1), 378–398.

Hamada, A., Takayabu, Y. N., Liu, C., & Zipser, E. J. (2015). Weak linkage between the heaviest rainfall and tallest storms. *Nature Communications*, *6*, 6213.

Islam, T., Srivastava, P. K., Rico-Ramirez, M. A., Dai, Q., Han, D., & Gupta, M. (2014). An exploratory investigation of an Adaptive Neuro Fuzzy Inference System (ANFIS) for estimating hydrometeors from TRMM/TMI in synergy with TRMM/PR. *Atmospheric Research*, *145*, 57–68.

Kidd, C., Matsui, T., Chern, J., Mohr, K., Kummerow, C., & Randel, D. (2016). Global precipitation estimates from cross-track passive microwave observations using a physically based retrieval scheme. *Journal of Hydrometeorology*, *17*(1), 383–400.

Kongoli, C., Meng, H., Dong, J., & Ferraro, R. (2015). A snowfall detection algorithm over land utilizing high-frequency passive microwave measurements Application to ATMS. *Journal of Geophysical Research: Atmospheres*, *120*, 1918–1932. https://doi.org/10.1002/2014JD022427

Koster, R. D., Brocca, L., Crow, W. T., Burgin, M. S., & De Lannoy, G. J. (2016). Precipitation estimation using L-band and C-band soil moisture retrievals. *Water Resources Research*, *52*(9), 7213–7225.

Kummerow, C., Hong, Y., Olson, W., Yang, S., Adler, R., McCollum, J., et al. (2001). The evolution of the Goddard Profiling Algorithm (GPROF) for rainfall estimation from passive microwave sensors. *Journal of Applied Meteorology*, *40*(11), 1801–1820.

Kummerow, C. D., Randel, D. L., Kulie, M., Wang, N.-Y., Ferraro, R., Joseph Munchak, S., & Petkovic, V. (2015). The evolution of the Goddard profiling algorithm to a fully parametric scheme. *Journal of Atmospheric and Oceanic Technology*, *32*(12), 2265–2280.

Laviola, S., & Levizzani, V. (2011). The 183-WSL fast rain rate retrieval algorithm: Part I: Retrieval design. *Atmospheric Research*, *99*(3), 443–461.

Liu, G. (1998). A fast and accurate model for microwave radiance calculations. *Journal of the Meteorological Society of Japan*, *76*(2), 335–343.

Liu, G., & Curry, J. A. (1992). Retrieval of precipitation from satellite microwave measurement using both emission and scattering. *Journal of Geophysical Research*, *97*(D9), 9959–9974.

Liu, C., & Zipser, E. J. (2009). "Warm rain" in the tropics: Seasonal and regional distributions based on 9 yr of TRMM data. *Journal of Climate*, *22*(3), 767–779.

McCollum, J. R., & Ferraro, R. R. (2003). Next generation of NOAA/NESDIS TMI, SSM/I, and AMSR-E microwave land rainfall algorithms. *Journal of Geophysical Research*, *108*(D8), 8382. https://doi.org/10.1029/2001JD001512

Miller, D. A., & White, R. A. (1998). A conterminous United States multilayer soil characteristics dataset for regional climate and hydrology modeling. *Earth Interactions*, *2*(2), 1–26.

Pellarin, T., Louvet, S., Gruhier, C., Quantin, G., & Legout, C. (2013). A simple and effective method for correcting soil moisture and precipitation estimates using AMSR-E measurements. *Remote Sensing of Environment*, *136*, 28–36.

Petty, G. W. (1995). The status of satellite-based rainfall estimation over land. *Remote Sensing of Environment*, *51*(1), 125–137.

Petty, G. W., & Li, K. (2013). Improved passive microwave retrievals of rain rate over land and ocean. Part II: Validation and intercomparison. *Journal of Atmospheric and Oceanic Technology*, *30*(11), 2509–2526.

Reynolds, C., Jackson, T., & Rawls, W. (2000). Estimating soil water-holding capacities by linking the Food and Agriculture Organization soil map of the world with global pedon databases and continuous pedotransfer functions. *Water Resources Research*, *36*(12), 3653–3662.

Sano, P., Casella, D., Mugnai, A., Schiavon, G., Smith, E. A., & Tripoli, G. J. (2013). Transitioning from CRD to CDRD in Bayesian retrieval of rainfall from satellite passive microwave measurements: Part 1. Algorithm description and testing. *IEEE Transactions on Geoscience and Remote Sensing*, *51*(7), 4119–4143.

Seo, E.-K., Yang, S.-D., Grecu, M., Ryu, G.-H., Liu, G., Hristova-Veleva, S., et al. (2016). Optimization of cloud-radiation databases for passive microwave precipitation retrievals over ocean. *Journal of Atmospheric and Oceanic Technology*, *33*(8), 1649–1671.

Seto, S., Iguchi, T., & Oki, T. (2013). The basic performance of a precipitation retrieval algorithm for the global precipitation measurement mission's single/dual-frequency radar measurements. *IEEE Transactions on Geoscience and Remote Sensing*, *51*(12), 5239–5251.

Sohn, B., Ryu, G.-H., Song, H.-J., & Ou, M.-L. (2013). Characteristic features of warm-type rain producing heavy rainfall over the Korean Peninsula inferred from TRMM measurements. *Monthly Weather Review*, *141*(11), 3873–3888.

Staelin, D. H., & Chen, F. W. (2000). Precipitation observations near 54 and 183 GHz using the NOAA-15 satellite. *IEEE Transactions on Geoscience and Remote Sensing*, *38*(5), 2322–2332.

Tian, Y., Peters-Lidard, C. D., Harrison, K. W., You, Y., Ringerud, S., Kumar, S., & Turk, F. J. (2015). An examination of methods for estimating land surface microwave emissivity. *Journal of Geophysical Research: Atmospheres*, *120*, 11,114–11,128. https://doi.org/10.1002/2015JD023582

Turk, F. J., Haddad, Z., & You, Y. (2016). Estimating nonraining surface parameters to assist GPM constellation radiometer precipitation algorithms. *Journal of Atmospheric and Oceanic Technology*, *33*(7), 1333–1353.

Wang, N.-Y., Liu, C., Ferraro, R., Wolff, D., Zipser, E., & Kummerow, C. (2009). TRMM 2A12 land precipitation product-status and future plans. *Journal of the Meteorological Society of Japan*, *87*, 237–253.

Wilheit, T. T. (1986). Some comments on passive microwave measurement of rain. *Bulletin of the American Meteorological Society*, *67*(10), 1226–1232.

Yang, S., Hawkins, J., & Richardson, K. (2014). The improved NRL tropical cyclone monitoring system with a unified microwave brightness temperature calibration scheme. *Radio Science*, *6*(5), 4563–4581.

Yang, S., Weng, F., Yan, B., Sun, N., & Goldberg, M. (2011). Special Sensor Microwave Imager (SSM/I) intersensor calibration using a simultaneous conical overpass technique. *Journal of Applied Meteorology and Climatology*, *50*(1), 77–95.

You, Y., & Liu, G. (2012). The relationship between surface rainrate and water paths and its implications to satellite rainrate retrieval. *Journal of Geophysical Research*, *117*, D12203. https://doi.org/10.1029/2010JD015345

You, Y., Liu, G., Wang, Y., & Cao, J. (2011). On the sensitivity of Tropical Rainfall Measuring Mission (TRMM) Microwave Imager channels to overland rainfall. *Journal of Geophysical Research*, *116*, D12203. https://doi.org/1029/2010JD015345

You, Y., Peters-Lidard, C., Turk, J., Ringerud, S., & Yang, S. (2017). Improving overland precipitation retrieval with brightness temperature temporal variation. *Journal of Hydrometeorology*, *18*(9), 2355–2383.

You, Y., Turk, F. J., Haddad, Z. S., Li, L., & Liu, G. (2014). Principal components of multifrequency microwave land surface emissivities. Part II: Effects of previous-time precipitation. *Journal of Hydrometeorology*, *15*(1), 20–37.

You, Y., Wang, N.-Y., & Ferraro, R. (2015). A prototype precipitation retrieval algorithm over land using passive microwave observations stratified by surface condition and precipitation vertical structure. *Journal of Geophysical Research: Atmospheres*, *120*, 5295–5315. https://doi.org/10.1002/2014JD022534

You, Y., Wang, N.-Y., Ferraro, R., & Meyers, P. (2016). A prototype precipitation retrieval algorithm over Land for ATMS. *Journal of Hydrometeorology*, *17*(5), 1601–1621.

You, Y., Wang, N.-Y., Ferraro, R., & Rudlosky, S. (2017). Quantifying the snowfall detection performance of the GPM microwave imager channels over land. *Journal of Hydrometeorology*, *18*(3), 729–751.

Zhang, J., Howard, K., Langston, C., Kaney, B., Qi, Y., Tang, L., et al. (2016). Multi-Radar Multi-Sensor (MRMS) quantitative precipitation estimation: Initial operating capabilities. *Bulletin of the American Meteorological Society*, *97*(4), 621–638.